Subtle Roles of Sb and S in Regulating the Thermoelectric Properties of N-Type PbTe to High Performance

*Gangjian Tan, Constantinos C. Stoumpos, Si Wang, Trevor P. Bailey, Li-Dong Zhao, Ctirad Uher, and Mercouri G. Kanatzidis**

A high *ZT* (thermoelectric figure of merit) of ≈1.4 at 900 K for n-type PbTe is reported, through modifying its electrical and thermal properties by incorporating Sb and S, respectively. Sb is confirmed to be an amphoteric dopant in PbTe, filling Te vacancies at low doping levels (<1%), exceeding which it enters into Pb sites. It is found that Sb-doped PbTe exhibits much higher carrier mobility than similar Bi-doped materials, and accordingly, delivers higher power factors and superior *ZT*. The enhanced electronic transport is attributed to the elimination of Te vacancies, which appear to strongly scatter n-type charge carriers. Building on this result, the *ZT* of $Pb_{0.9875}Sb_{0.0125}Te$ is further enhanced by alloying S into the Te sublattice. The introduction of S opens the bandgap of PbTe, which suppresses bipolar conduction while simultaneously increasing the electron concentration and electrical conductivity. Furthermore, it introduces point defects and induces second phase nanostructuring, which lowers the lattice thermal conductivity to ≈0.5 W m^{-1} K^{-1} at 900 K, making this material a robust candidate for high-temperature (500–900 K) thermoelectric applications. It is anticipated that the insights provided here will be an important addition to the growing arsenal of strategies for optimizing the performance of thermoelectric materials.

1. Introduction

Thermoelectric materials can convert heat to electricity and are gaining increasing attention as a possible means to increase the efficiency of energy-generating processes.[1–4] The effectiveness of a thermoelectric material is evaluated by the dimensionless figure of merit $ZT = S^2\sigma T/\kappa_{tot} = S^2\sigma T/(\kappa_{ele} + \kappa_{lat})$, where S is the Seebeck coefficient, σ is the electrical conductivity, T is the absolute temperature, and κ_{tot} is the total thermal conductivity, which is a sum of the electronic (κ_{ele}) and lattice (κ_{lat}) contributions. S, σ, and κ_{ele} are closely related to each other through carrier concentration (n). Thus, carrier concentration optimization by aliovalent ion doping is an effective strategy for maximizing the ZT (ZT_{max}) of a given material.[5,6] Additionally, it is necessary to improve the thermoelectric quality factor β, which can be expressed as $\beta = T^{5/2}U/\kappa_{lat}$.[7,8] In the expression of β, U denotes the weighted mobility for the carriers which have mobility μ, effective mass m^*, and which populate N_V equivalent valleys of the band structure: $U = N_V(m^*)^{3/2}\mu$. Thus, larger N_V, m^*, and μ, but smaller κ_{lat}, is required to achieve the highest possible ZT_{max}.

PbTe is the top-performing thermoelectric material in the temperature interval of 500–900 K.[1,9–12] Although this material was regarded as high-symmetry rocksalt-type crystal structure, recent studies utilizing synchrotron powder X-ray diffraction (XRD) technique show that it actually contains certain degree of cationic disorder (emphanisis) and defects which are partly responsible for its intrinsically low thermal conductivity.[13–16] Moreover, the κ_{lat} of PbTe can be further decreased by synergistic alloying (i.e., PbS,[17] PbSe,[18] SnTe,[19] etc.) and nanostructuring (i.e., CaTe,[20] SrTe,[10,11] BaTe,[20] ZnTe,[21] etc.).

In addition to having intrinsically low κ_{lat}, PbTe also features a unique band structure that endows it with large U values. P-type PbTe is a particularly good thermoelectric because of the presence of two valence bands, namely a primary light hole band at the L point and a second heavy hole band at the Σ point, separated by an energy difference (ΔE_V) of ≈0.15–0.20 eV at 300 K (see Figure S1a in the Supporting Information).[22,23] With increasing temperature or upon alloying with specific elements (Cd,[24] Mg,[25,26] Mn,[27,28] etc.), ΔE_V can be further decreased to within a few k_BT (k_B is the Boltzmann constant, T is the absolute temperature), leading to effective valence band convergence, i.e., an increase of N_V. By contrast, in n-type PbTe, only the light conduction band with small m^* at L point contributes

Dr. G. Tan, Dr. C. C. Stoumpos, Prof. M. G. Kanatzidis
Department of Chemistry
Northwestern University
Evanston, IL 60208, USA
E-mail: m-kanatzidis@northwestern.edu

S. Wang, T. P. Bailey, Prof. C. Uher
Department of Physics
University of Michigan
Ann Arbor, MI 48109, USA

S. Wang
State Key Laboratory of Advanced Technology for Materials Synthesis and Processing
Wuhan University of Technology
Wuhan 430070, China

Prof. L.-D. Zhao
School of Materials Science and Engineering
Beihang University
Beijing 100191, China

The ORCID identification number(s) for the author(s) of this article can be found under https://doi.org/10.1002/aenm.201700099.

DOI: 10.1002/aenm.201700099

to the electron transport.[29] The consequence is that, under equal concentration of electrons or holes (n), the Seebeck coefficient of n-type PbTe is inferior to its p-type counterpart, especially at high doping levels ($n > 2 \times 10^{19}$ cm^{-3}) where the heavy Σ valence band becomes available,[30,31] Figure S1b (Supporting Information).

The difference in availability of large N_V between n- and p-type PbTe leads to a significant ZT mismatch. Specifically, $ZT > 1.8$ is now readily achievable for heavily doped p-type PbTe,[10–12,17,25,32] while much lower ZT values of around 1.1 are commonly reported for n-type materials.[33–37] It is well known that thermoelectric modules require both p- and n-type materials with equally high performance and comparable thermomechanical properties.[38] Accordingly, it is necessary to develop more efficient n-type PbTe-based materials to match the performance of the existing p-type systems.

The purpose of this study was to systematically improve the thermoelectric performance of n-type PbTe by optimizing carrier concentration using Sb and Bi dopants, and by enhancing m^* and κ_{lat} through PbS alloying/nanostructuring. Consistent with previous reports, it was found that Bi preferably occupies Pb sites at all doping levels within the solubility limit, acting as an efficient n-type dopant.[39] Conversely, we observe that at low doping levels (<1 mol%), Sb partially enters Te sites (p-type dopant) and at higher concentrations (>1 mol%) it tends to replace Pb atoms (n-type dopant). For both Bi- and Sb-doped n-type PbTe, the Seebeck coefficient—carrier concentration relationship agrees well with the theoretical Pisarenko plot assuming the single band model. However, Sb-doped PbTe features much higher μ and thus higher power factor than similar Bi-doped systems with similar carrier concentration). An amount of 1.25% Sb dopant in PbTe gives a maximum ZT of ≈1.1 at 800 K.

Alloying with PbS increases the bandgap of PbTe thereby largely suppressing the bipolar diffusion at elevated temperature. We also observe that the introduction of PbS increases the carrier concentration n of $Pb_{0.9875}Sb_{0.0125}Te$. Furthermore, the effective mass of electrons (m^*) of the Sb-doped PbTe–PbS samples is increased with respect to pure PbTe, which helps achieve high Seebeck coefficients despite the increased n. Coupled with the decreased κ_{lat} caused by point defect scattering created by S alloying at Te sites, as well as nanostructured PbS, the ZT value of $Pb_{0.9875}Sb_{0.0125}Te_{0.88}S_{0.12}$ is enhanced to ≈1.4 at 900 K, which is among the best values for n-type PbTe-based materials.

2. Results and Discussion

2.1. Atomic Substitution of Bi and Sb in PbTe

Figures S2 and S3 (Supporting Information) show the conventional and synchrotron powder XRD patterns for $Pb_{1-x}M_xTe$ (M = Bi or Sb), respectively. All samples are single phase compounds crystalizing in the rock salt PbTe structure within the detection limit of laboratory X-ray instrument. We have performed Rietveld refinement for all the $Pb_{1-x}M_xTe$ samples using synchrotron diffraction data and **Figure 1**a shows a representative example for the sample $Pb_{1-x}Sb_xTe$ (x = 1%). The

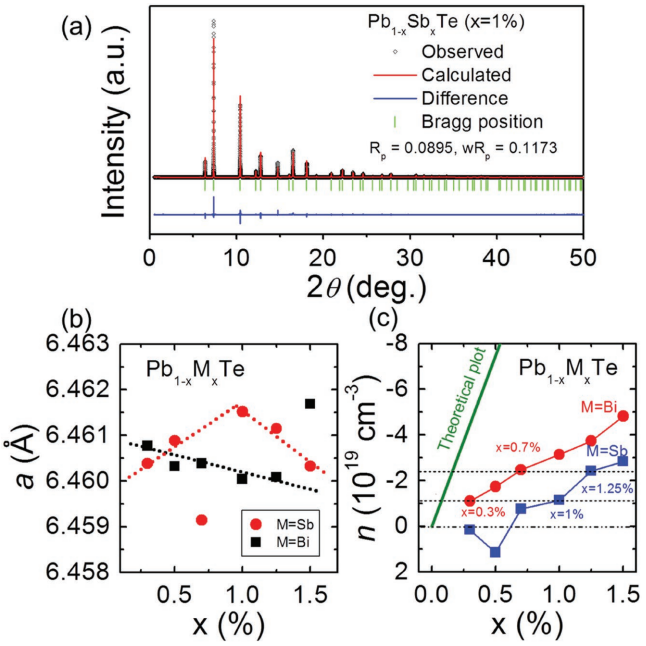

Figure 1. a) Representative Rietveld refinement of $Pb_{1-x}Sb_xTe$ (x = 1%) against synchrotron diffraction data. b) Lattice parameters a as a function of doping fractions of Bi and Sb. The lines are guide to eyes. c) Room temperature carrier concentration n as a function of x for $Pb_{1-x}M_xTe$ (M = Bi, Sb). Positive n means holes as the majority carriers, while negative n suggests electrons as the majority carriers. The straight line denotes the theoretical n by consuming one Bi (or Sb) substitution for Pb generates one free electron.

lattice parameters (a), obtained through this Rietveld refinement method, as a function of dopant concentration (x) for $Pb_{1-x}M_xTe$ (M = Bi or Sb) are shown in Figure 1b. In the case of Bi-doped PbTe, a decreases almost linearly with increasing x, which is consistent with the smaller radius of Bi^{3+} (≈1.08 Å) in comparison to Pb^{2+} (≈1.20 Å) and confirms the successful substitution of Bi for Pb in PbTe. However, for Sb-doped PbTe, a first roughly increases with increasing x up to 1%, followed by linear decrease afterward.

Previous experimental and theoretical studies demonstrate that Sb is an amphoteric dopant in PbTe, using various techniques beyond crystallography.[40,41] In other words, it can reside at either Pb or Te sites of the NaCl-type lattice, depending on the amount incorporated into the PbTe matrix. Intuitively, if Sb goes to the Pb sites, then the lattice parameter of PbTe should decrease with increasing Sb concentration, since the radius of Sb^{3+} (≈0.92 Å) is smaller than that of Pb^{2+} (≈1.20 Å). Likewise, if Sb replaces Te atoms, the lattice of PbTe should shrink, since the radius of Sb^{3-} (≈2.08 Å) is smaller than that of Te^{2-} (≈2.10 Å).[42] A rational interpretation of the data shown in Figure 1b is that the lattice expansion of PbTe upon Sb addition below 1% is due to the partial filling of Te vacancies by Sb atoms. At higher concentrations of Sb (x > 1%) the Te vacancies are saturated, and Sb prefers to occupy the Pb sites (Sb^{3+} state), thus shrinking the lattice. Thus, our study confirms a previous conclusion that Sb is an amphoteric dopant in PbTe.[40,41]

The different chemical states of Bi and Sb in PbTe are also reflected in Figure 1c, which shows the relationship between carrier density and dopant concentration. Even at the lowest doping concentration (0.3%) of Bi in PbTe there is an electron concentration (n) as high as -1.1×10^{19} cm^{-3} at room temperature, and n increases linearly with increasing Bi concentration, reaching -4.8×10^{19} cm^{-3} for $x = 1.5\%$. This provides strong evidence that Bi is an electron donor at all doping levels in PbTe, and agrees well with previous studies.[39] By contrast, the majority carriers prove to be holes for the $Pb_{1-x}Sb_xTe$ samples when $x < 0.5\%$, which we attribute to Sb atoms filling Te vacancies and acting as electron acceptors. When $x > 0.5\%$, $Pb_{1-x}Sb_xTe$ become dominated by n-type carriers, and n increases monotonously with increasing x, since Sb preferably starts to replace Pb atoms within this composition range and acts as an electron donor. Moreover, when the two systems have identical dopant concentrations, the n of $Pb_{1-x}Bi_xTe$ is always larger than that of $Pb_{1-x}Sb_xTe$. For example, 0.3% (or 0.7%) Bi doping gives the same n as 1% (or 1.25%) Sb, as indicated by the dotted lines in Figure 1c. Note that in both cases, the measured Hall concentrations are lower than the predicted values (denoted by the olive line), which is calculated with assumption that each dopant atom generates one free electron. This is probably suggests the presence of a second phase containing these elements.

2.2. Subtle Role of Sb in Enhancing the Performance of PbTe

The electrical conductivity (σ) and Seebeck coefficient (S) as a function of temperature for $Pb_{1-x}M_xTe$ (M = Bi, Sb) are shown in **Figure 2**. In both cases, σ increases while S decreases systematically with increasing doping concentration of M because

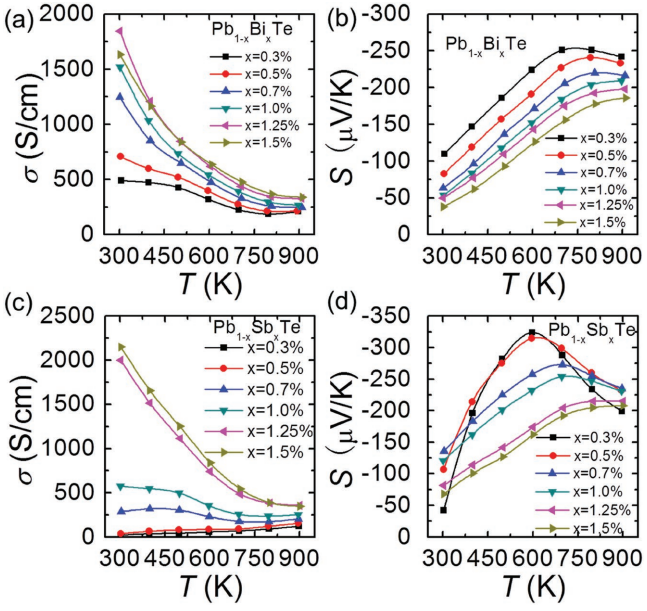

Figure 2. a) Temperature dependent electrical conductivity and b) Seebeck coefficient for $Pb_{1-x}Bi_xTe$. c) Temperature dependent electrical conductivity and d) Seebeck coefficient for $Pb_{1-x}Sb_xTe$.

of the enhanced carrier density (Figure 1c), although the $Pb_{1-x}Sb_xTe$ ($x = 0.3\%$ and 0.5%) samples are exceptional. In these two samples, at room temperature, the Hall carrier concentrations are positive (Figure 1c) but the Seebeck coefficients are negative (Figure 2d), indicating the simultaneous presence of two types of carriers (electrons and holes) giving rise to the complex relationship between n and S. Also, the negative Seebeck coefficient but positive Hall coefficient in the intrinsic semiconductor of PbTe suggests that its electron mobility is larger than hole mobility around room temperature, which is consistent with previous report.[43]

Figure 3a shows the high temperature Hall measurement data of $Pb_{1-x}M_xTe$ (M = Bi, Sb; $x = 0.3\%$, 0.7%, 1.25%). In the inset of Figure 3a the Hall data show an apparent p to n transition occurring around 350 K for the sample $Pb_{0.097}Sb_{0.003}Te$, which supports the presence of two carriers (electrons and holes) with comparable concentration.[40] For all other compositions, the Hall coefficient (R_H) remains almost constant before rising at elevated temperature due to the intrinsic excitation of minority carriers (bipolar diffusion). One could also note that the bipolar diffusion is significantly inhibited because of the heavy doping levels achieved. The weak temperature dependence of R_H in n-type PbTe also suggests a single band conduction behavior, as was discussed in the Introduction.

Figure 3b shows the room temperature Seebeck coefficient as a function of carrier concentration for $Pb_{1-x}M_xTe$ (M = Bi, Sb; the samples doped with 0.3% and 0.7% Sb are excluded because of the mixed carriers). The solid line is the theoretical Pisarenko plot for n-type PbTe with electron effective mass of 0.25 m_e (m_e is the free electron mass).[31] Clearly, in both cases, the experimental data agree well with the theoretical predictions, suggesting that both Sb and Bi are pure dopants in PbTe, which do not significantly influence the conduction band structure. Indeed, with similar n, the Seebeck coefficients of Bi- and Sb-doped PbTe are similar over the entire measurement temperature range of 300–900 K, as shown in Figure 3c. However, there is considerable difference in electrical conductivity between them (inset of Figure 3d). For example, at 300 K, σ of 1.25% Sb-doped PbTe (≈2000 S cm^{-1}) is 60% larger than that of 0.7% Bi-doped one (1250 S cm^{-1}), while their n is quite close (2.4 vs 2.5×10^{19} cm^{-3} at 300 K). The significantly higher electrical conductivity of $Pb_{1-x}Sb_xTe$ leads to much larger power factors compared to the $Pb_{1-x}Bi_xTe$ samples (Figure S4, Supporting Information).

The difference in electrical conductivity of Sb- and Bi-doped PbTe arises from the difference in mobility, see Figure 3d. One plausible explanation could be that in compounds with high dielectric permittivity like PbTe, the efficiency of the carrier scattering by charged centers (i.e., Sb_{Pb}^- or Bi_{Pb}^-) is significantly lower when compared to lattice deformations induced by point defects (i.e., Te vacancies).[44,45] Therefore, in Sb-doped PbTe, where Te vacancies are filled with Sb atoms, there are less carrier scatterings and thus, greater carrier mobilities. We also compared the temperature dependence of electron mobilities of Sb-doped PbTe and PbSe with similar carrier concentrations,[46] as shown in Figure 3d. It is noted that they behave quite close mobilities over the entire temperature range from 300 to 700 K. This is not surprising because PbTe and PbSe have comparable

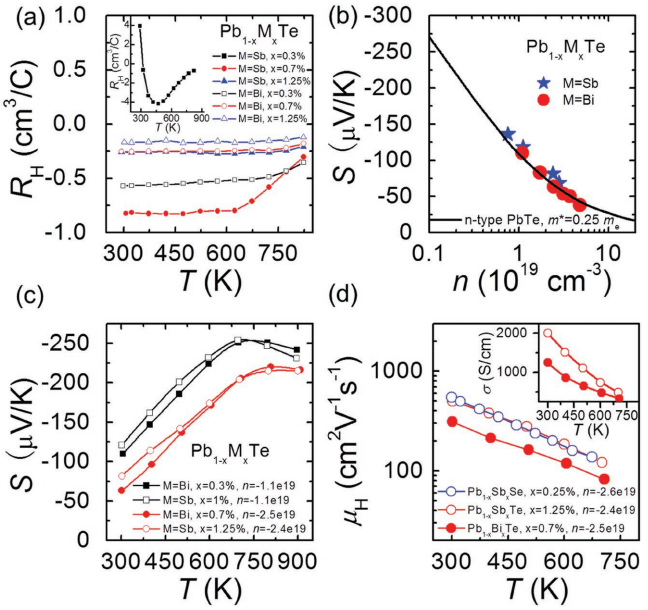

Figure 3. a) High temperature Hall coefficients of $Pb_{1-x}Bi_xTe$ (M = Bi, Sb). b) Room temperature Seebeck coefficient as a function of carrier concentration for $Pb_{1-x}Bi_xTe$ (M = Bi, Sb). The solid curve is the theoretical Pisarenko plot for n-type PbTe with effective mass of electrons of 0.25 m_e.[31] Comparison of c) Seebeck coefficient, d) carrier mobility and electrical conductivity (inset of (d)) of $Pb_{1-x}Bi_xTe$ and $Pb_{1-x}Sb_xTe$ with equal carrier concentrations. 1.1e19, 2.4e19, and 2.5e19 denote carrier concentrations of 1.1, 2.4, and 2.5×10^{19} cm^{-3}, respectively. The blue symbols in (d) represent the temperature dependence of electron mobility for $Pb_{1-x}Sb_xSe$.[46]

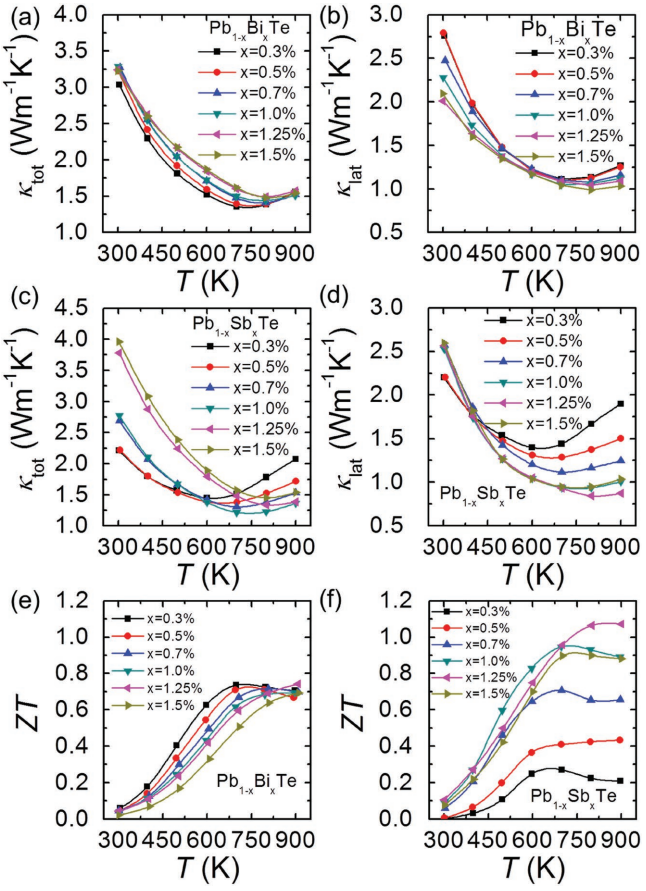

Figure 4. Temperature dependent a) total, and b) lattice thermal conductivities, and e) ZT values for $Pb_{1-x}Bi_xTe$. Temperature dependent c) total and d) lattice thermal conductivities, and f) ZT values for $Pb_{1-x}Sb_xTe$.

magnitudes of both bandgap and conduction band effective mass.[47]

Figure 4a,c shows the total thermal conductivity (κ_{tot}) as a function of temperature for $Pb_{1-x}Bi_xTe$ and $Pb_{1-x}Sb_xTe$, respectively. In both cases, κ_{tot} decreases with increasing temperature but increases with increasing doping fractions. As expected, the lattice thermal conductivity (κ_{lat}) of $Pb_{1-x}Bi_xTe$ decreases systematically with increasing Bi concentration due an increase in point defect scattering (Figure 4b). In contrast, κ_{lat} of $Pb_{1-x}Sb_xTe$ has very weak composition dependence, and the room temperature values range between 2.2 and 2.5 W m^{-1} K^{-1} with varying x (Figure 4d). It should be mentioned here that at low doping fractions (x = 0.3% and 0.5%, for example), Sb-doped PbTe behaves much lower κ_{lat} (≈2.2 W m^{-1} K^{-1}) than those of Bi-doped one (≈2.8 W m^{-1} K^{-1}) at room temperature. To some extent this is ascribed to the fact that in the former Sb preferably occupies Te vacancies. Owing to the ≈100% mass difference between Sb atoms and Te vacancies, this leads to the strongest phonon scattering rate.[1–3,12,48–50]

We also note that the bipolar diffusion (the rising of κ_{lat}, Figure 4b,d) is greatly inhibited with increasing x in both Bi- and Sb-doped PbTe, consistent with the Hall study presented in Figure 3a. However, at elevated temperature, the lowest κ_{lat} are comparable for those two series of compounds (≈1.0 W m^{-1} K^{-1} for $Pb_{1-x}Bi_xTe$ and ≈0.85 W m^{-1} K^{-1} for $Pb_{1-x}Sb_xTe$ at 800 K) and are much higher than the theoretically calculated minimum thermal conductivity of ≈0.36 W m^{-1} K^{-1} for PbTe,[51] indicating that there is still room to lower the κ_{lat} using other state-of-the-art strategies such as alloying and/or nanostructuring,[32,49,52–56] which are discussed below.

Figure 4e,f shows the temperature dependence of ZT values for $Pb_{1-x}Bi_xTe$ and $Pb_{1-x}Sb_xTe$, respectively. In the case of $Pb_{1-x}Bi_xTe$, the lowest doping fraction yields the best performance with the highest ZT value of ≈0.75 at 700 K. Sb-doped PbTe has considerably larger ZT values approaching 1.1 at 800 K. This can be attributed to the enhanced charge carrier mobility in the Sb-doped systems, which provide greater power factors and consequently, superior thermoelectric performance.

2.3. The Effects of S Alloying on the Performance of PbTe

2.3.1. Phase Purity and Bandgap of 1.25% Sb-Doped PbTe–PbS Alloys

Figure S5a (Supporting Information) shows the powder XRD patterns of $Pb_{0.9875}Sb_{0.0125}Te_{1-y}S_y$ (y = 0–0.16). No observable second phase can be detected within the X-ray limit except for the y = 0.12 and 0.16 samples, at which point PbS impurities can be identified, as shown in Figure S5b (Supporting Information). The infrared absorption spectroscopy of nondoped $PbTe_{1-y}S_y$ (y = 0–0.16) with low carrier concentration is plotted

in Figure S5c (Supporting Information), and an evident blueshift of the absorption edge with increasing S concentration was observed, indicating increased band gap as shown in Figure S5d (Supporting Information). The enlargement of the bandgap of PbTe with increasing y is expected, since PbS has a larger bandgap (0.41 eV at 300 K) than PbTe (0.29 eV at 300 K).[57] However, the experimental bandgaps are apparently lower than estimated from Vegard's law (solid line in Figure S5d in the Supporting Information), which suggests that PbTe–PbS is not a complete solid solution, which is consistent with previous studies.[17,35,58,59]

2.3.2. Electrical Properties of $Pb_{0.9875}Sb_{0.0125}Te_{1-y}S_y$

Figure 5a,b shows the electrical conductivity and Seebeck coefficient as a function of temperature for $Pb_{0.9875}Sb_{0.0125}Te_{1-y}S_y$, respectively. Theoretically, S substitution for Te in PbTe would result in decrease of mobility because of the additional point defects, but should have no influence on the carrier concentration because S is isoelectric to Te. Therefore, one would expect a gradual decrease of electrical conductivity, as well as an unchanged Seebeck coefficient, as S is increased from 0% to 16% in the PbTe matrix. However, we find that the electrical conductivity of $Pb_{0.9875}Sb_{0.0125}Te_{1-y}S_y$ shows negligible changes with increasing sulfur concentration while the Seebeck coefficient is decreased, especially at low temperatures.

To find out why the incorporation of S does not affect the electrical conductivity and Seebeck coefficient, we carried out Hall Effect measurements, to determine if the carrier concentrations remained unchanged. The room temperature carrier concentration and mobility of $Pb_{0.9875}Sb_{0.0125}Te_{1-y}S_y$ as a function of S concentration are shown in Figure 5c,d, respectively. As expected, we observe a decreasing trend in the mobility of $Pb_{0.9875}Sb_{0.0125}Te_{1-y}S_y$ with increasing y due to enhanced alloy scattering. However, unexpectedly, we observe a substantial increase of carrier concentration with increasing fraction of sulfur, which compensates for the decrease in carrier mobility to retain the high electrical conductivity. We argue that the incorporation of PbS shrinks the PbTe lattice and makes the Te site unfavorable form occupation. Thus only Pb site is available to host the Sb atoms. The higher carrier concentration also accounts for the decrease of Seebeck coefficient around room temperature.

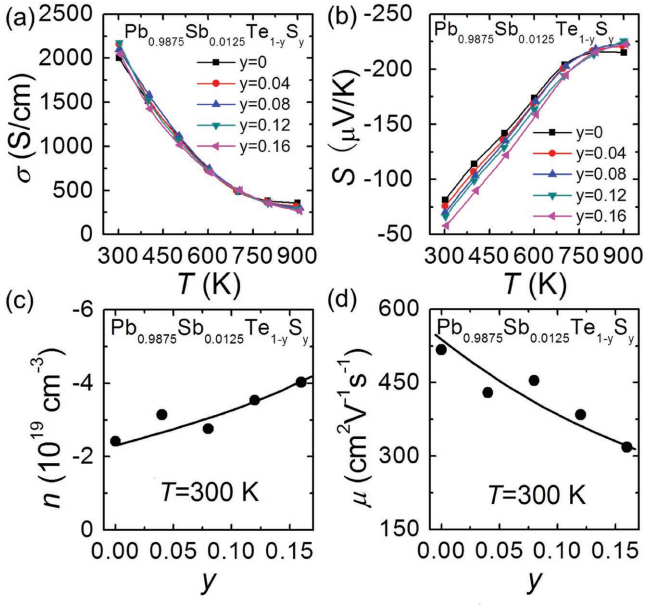

Figure 5. a) Temperature dependent electrical conductivity and b) Seebeck coefficient for $Pb_{0.9875}Sb_{0.0125}Te_{1-y}S_y$. Room temperature c) carrier concentration and d) mobility as a function of S alloying fraction.

2.3.3. Thermal Properties and Bipolar Diffusion Suppression of $Pb_{0.9875}Sb_{0.0125}Te_{1-y}S_y$

Figure 6a,b shows the total and lattice thermal conductivities as a function of temperature for $Pb_{0.9875}Sb_{0.0125}Te_{1-y}S_y$, respectively, both of which decrease with increasing concentration of S. The lowest lattice thermal conductivity is ≈0.5 W m^{-1} K^{-1} at ≈900 K for the $y = 0.12$ sample, which approaches the theoretical minimum thermal conductivity of ≈0.36 W m^{-1} K^{-1} for PbTe.[51] Figure 6c plots the room temperature lattice thermal conductivities of $Pb_{0.9875}Sb_{0.0125}Te_{1-y}S_y$ as a function of S doping concentration y, although the modified Klemens model[60] (solid line, see refs. [32,61,62] for details of simulations) only fits the experimental results when $y = 0.04$. At high sulfur concentration levels we note that the experimental lattice thermal conductivities fall below the simulated line. This indicates that an additional

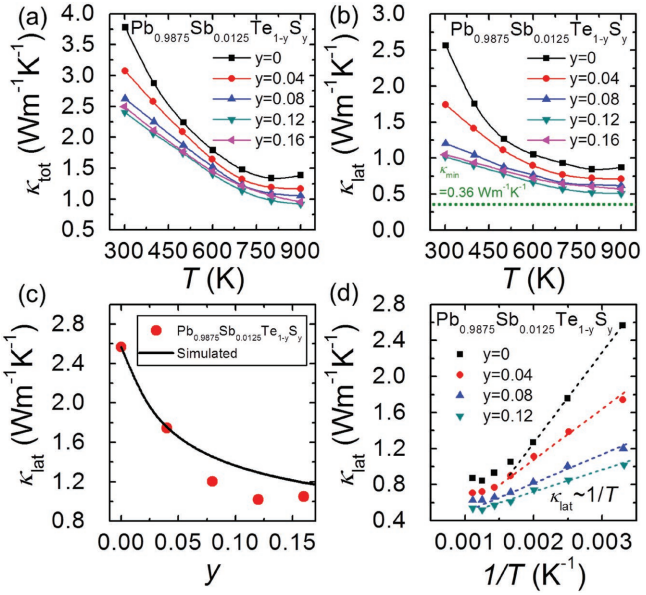

Figure 6. Temperature dependent a) total and b) lattice thermal conductivities for $Pb_{0.9875}Sb_{0.0125}Te_{1-y}S_y$. The dotted line in (b) denotes the theoretical minimum thermal conductivity (≈0.36 W m^{-1} K^{-1}) for PbTe-based material.[51] c) Room temperature lattice thermal conductivities as a function of S alloying fraction y. The solid line presents the simulated lattice thermal conductivities of PbTe–PbS using a modified Klemens' model.[60] d) Lattice thermal conductivities of $Pb_{0.9875}Sb_{0.0125}Te_{1-y}S_y$ as a function of reciprocal temperature. The dotted lines denote a $1/T$ dependence of lattice thermal conductivity. The deviation of lattice thermal conductivity from such a relationship indicates the onset of bipolar conduction.

mechanism, other than point defect scattering, is influencing the thermal conductivity of the $Pb_{0.9875}Sb_{0.0125}Te_{1-y}S_y$ samples. Similar to previous reports,[17,47,58,59] we believe that phase separation at the nanometer scale due to phase immiscibility in $PbTe_{1-x}S_x$ is responsible for the exceptionally low thermal conductivity.

For semiconductors, where Umklapp scattering is the predominant phonon scattering mechanism, their lattice thermal conductivity should be reciprocally proportional to the temperature prior to the onset of bipolar diffusion,[6,63,64] which has been confirmed previously for PbTe.[25,32] Figure 6d shows κ_{lat} as a function of $1/T$ for $Pb_{0.9875}Sb_{0.0125}Te_{1-y}S_y$, which clearly shows that bipolar diffusion is significantly suppressed for samples with higher S concentrations. This is likely due to both the increase in band gap (Figure S5d, Supporting Information) and carrier concentration (Figure 5c) as S concentration is increased, which will be addressed in greater detail below.

2.3.4. The Evolution of Band Structure for $PbTe_{1-y}S_y$

Figure 7a shows the high temperature Hall coefficient (R_H) measurement results on $Pb_{0.9875}Sb_{0.0125}Te_{1-y}S_y$. R_H is almost temperature independent in these heavily doped semiconductors, which agrees with the expected single-band-conduction behavior. Figure 7b plots the room temperature Seebeck coefficients as a function of carrier concentration for $Pb_{0.9875}Sb_{0.0125}Te_{1-y}S_y$. The black and red lines represent the theoretical Pisarenko plots for n-type PbTe and PbS, respectively.[31,65] N-type PbS should have a higher Seebeck coefficient than n-type PbTe (with identical carrier concentration) since the conduction band effective masses of PbS (0.39 m_e)[66] is much larger than that of PbTe (0.25 m_e).[31] One could see that the Seebeck coefficient data of $Pb_{0.9875}Sb_{0.0125}Te_{1-y}S_y$ lies in-between the black and the red lines, which suggests that there is a systematic change of the band structure of PbTe as PbS is introduced.

Although both PbTe and PbS adopt the same rocksalt-type crystal structure, the bandgap of PbS (≈0.41 eV) is substantially larger than that of PbTe (≈0.29 eV) at room temperature.[57,67] With increasing fraction of S added to PbTe, the bandgap gradually increases as the light hole valence band maxima of PbTe lowers its energy, while the energy of the heavy hole band remains unaffected, Figure 7c. This has been observed previously on the PbS-rich side of the PbTe–PbS system.[65] Since the conduction band effective mass of PbS is greater than that of PbTe,[31,66] the alloying of PbS also flattens the conduction band minima of PbTe for overall increased effective mass of electrons. The enlarged bandgap and increased effective mass of $PbTe_{1-y}S_y$ are responsible for the experimentally observed bipolar diffusion suppression (Figure 6d) and Seebeck coefficient enhancement (Figure 7b), respectively.

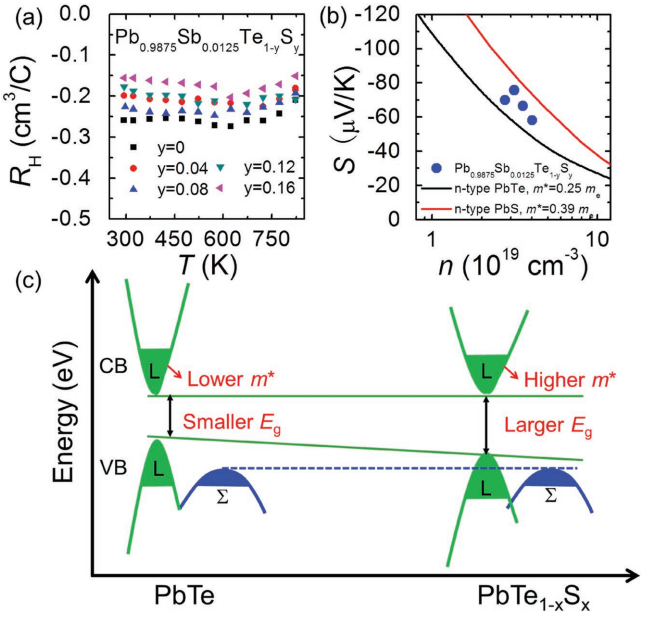

Figure 7. a) High temperature Hall coefficients of $Pb_{0.9875}Sb_{0.0125}Te_{1-y}S_y$. b) Room temperature Seebeck coefficient as a function of carrier concentration for $Pb_{0.9875}Sb_{0.0125}Te_{1-y}S_y$. The black and red lines denote the theoretical Pisarenko plots for n-type PbTe[31] with effective mass of electrons of 0.25 m_e and n-type PbS[66] with effective mass of electrons of 0.39 m_e, respectively. c) A schematic diagram showing the evolution of band structure of PbTe as the PbS alloying fraction is increased.

2.3.5. ZT Values of $Pb_{0.9875}Sb_{0.0125}Te_{1-y}S_y$

Figure 8a shows the temperature dependent ZT values for $Pb_{0.9875}Sb_{0.0125}Te_{1-y}S_y$. It is observed that ZT is greatly boosted by introducing an appropriate amount of S into the PbTe matrix, which can be attributed to the following combinational effects: (i) PbS shrinks the PbTe lattice and makes the Te site unfavorable form occupation. Thus only Pb site is available to host the Sb atoms, leading to an increase in n, combined with the (ii) enlarged bandgap for suppression of bipolar diffusion; (iii) it flattens the conduction band minima of PbTe, resulting in electrons with higher effective mass and thus, higher Seebeck coefficients; (iv) it decreases the thermal conductivity as a consequence of enhanced point defects scattering and second phase nanostructuring. As a result, the y = 0.12 sample displays the greatest ZT of ≈1.4 at ≈900 K, which outperforms many other n-type PbTe reported so far,[34–36] though this value is still lower than some other

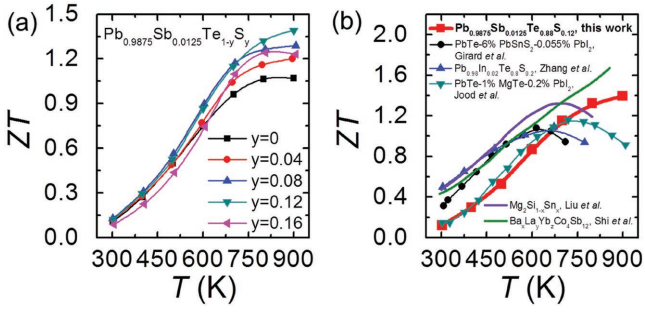

Figure 8. a) ZT values as a function of temperature for $Pb_{0.9875}Sb_{0.0125}Te_{1-y}S_y$. b) Comparison of ZT values of n-type PbTe in the present study with those in previous reports[34–36] and those of other state-of-the-art n-type thermoelectric materials, including triple-filled skutterudites $Ba_xLa_yYb_zCo_4Sb_{12}$ and $Mg_2Si_{1-x}Sn_x$ alloys.[68,69]

state-of-the-art n-type thermoelectric materials such as triple-filled skutterudite ($Ba_xLa_yYb_zCo_4Sb_{12}$)[68] and $Mg_2Si_{1-x}Sn_x$ alloy,[69] Figure 8b. We note that the high performance n-type PbTe sample demonstrated in this study is thermally stable, as demonstrated by the negligible changes of thermoelectric properties during the multiple heating-cooling cycles and after long-time vacuum annealing, Figure S6 (Supporting Information). This is important for its actual application in thermoelectric device.

3. Concluding Remarks

We demonstrated high thermoelectric performance ($ZT = 1.4$ at 900 K) in n-type Sb-doped and S-alloyed PbTe. Similar to Bi, Sb proves to have little influence on the electronic structure of PbTe. Furthermore, we have confirmed the amphoteric behavior of Sb as a dopant, namely it preferably fills Te vacancies at low doping levels (<1%), exceeding which it mostly goes to Pb site. By contrast, Bi replaces Pb at all doping levels within the solubility limit. The filling of Te vacancies by Sb atoms leads to much higher mobility (electrical conductivity) in comparison with $Pb_{1-x}Bi_xTe$ where Te site is not influenced, because Te vacancies are much stronger scattering centers than charged centers in PbTe. Thus, $Pb_{1-x}Sb_xTe$ has significantly larger ZT (≈1.1) than that of $Pb_{1-x}Bi_xTe$ (maxima $ZT \approx 0.75$).

Further enhancement of ZT of $Pb_{1-x}Sb_xTe$ is achieved through a partial substitution of Te by S. We show that the introduction of S leads to increased carrier concentration. Along with the bandgap enlargement by alloying larger bandgap PbS with PbTe, the bipolar diffusion is significantly suppressed. We also observe that the Seebeck coefficient of PbTe is increased by S alloying because PbS has larger effective mass of electrons than PbTe. Finally, a strong reduction of thermal conductivity of PbTe is obtained by S replacement for Te due to enhanced point defect scattering and second phase nanostructuring. Concurrently, a maximum ZT of ≈1.4 at ≈900 K is realized in 1.25% Sb-contained and 12% S-introduced PbTe, one of the best results for n-type PbTe-based thermoelectric material.

4. Experimental Section

Synthesis: Reagent chemicals were used as received: Pb wires (99.99%, American Elements, US), Bi shots (99.999%, American Elements, US), Sb shots (99.99%, American Elements, US), Te shots (99.999%, American Elements, US), and S flakes (99.999%, American Elements, US).

Weighing: High-purity single elements Pb, Bi, Sb, Te, and S were weighed according to the nominal compositions of $Pb_{1-x}M_xTe$ (M = Bi or Sb; x = 0.3%, 0.5%, 0.7%, 0.1%, 1.25%, and 1.5%) and $Pb_{0.9875}Sb_{0.0125}Te_{1-y}S_y$ (y = 0.04, 0.08, 0.12, and 0.16), and then put inside 13 mm diameter fused quartz tubes. The tubes were then evacuated to a residual pressure of ≈10^{-4} Torr and flame-sealed. For a typical experiment the following amounts were used: Pb (9.5236 g, 45.9633 mmol), Sb (0.0708 g, 0.5818 mmol), Te (5.2265 g, 40.9597 mmol), and S (0.1791 g, 5.5854 mmol) were used to prepare 15 g of $Pb_{0.9875}Sb_{0.0125}Te_{0.88}S_{0.12}$. Another series of undoped $PbTe_{1-x}S_x$ (x = 0–0.16) samples with low carrier concentrations were also made to probe the variation of bandgaps.

Melting: The loaded tubes were melted in computer controlled furnaces. The samples were slowly heated to 1373 K over 20 h, soaked at this temperature for 6 h, and then slowly cooled to 873 K in 2 h, dwelled at this temperature for another 12 h, and subsequently cooled to room temperature by switching off the furnace power. During the melting stage, the tubes were periodically shaken to promote the completion of the reaction between elements and ensure the sufficient homogeneity of the products.

Densification: The resultant ingots were crushed into fine powders in glove box filled with N_2 and then densified by spark plasma sintering (SPS) method (SPS-211LX, Fuji Electronic Industrial Co., Ltd.) at 823 K for 5 min in a 12.7 mm diameter graphite die under an axial compressive stress of 40 MPa in vacuum. Highly dense (>96.5% of theoretical density, Table S1, Supporting Information) disk-shaped pellets with dimensions of 12.7 mm diameter and 12 mm thickness were obtained. To induce nanostructuring in the PbTe–PbS system, based on their pseudobinary phase diagram,[58,70] the SPSed pellets of $Pb_{0.9875}Sb_{0.0125}Te_{1-y}S_y$ (y = 0.04, 0.08, 0.12, and 0.16) were further vacuum annealed at 673 K for 24 h before cutting into desired shapes for thermoelectric properties measurement.

X-Ray Diffraction: Samples pulverized with an agate mortar were used for powder XRD. The powder diffraction patterns were obtained using a Rigaku Miniflex600 powder X-ray diffractometer (Cu Kα graphite, λ = 1.5406 Å) operating at 40 kV/15 mA with a Kβ foil filter.

Synchrotron X-Ray Diffraction: High resolution synchrotron powder diffraction data were collected using beamline 11-BM at the Advanced Photon Source (APS), Argonne National Laboratory using an average wavelength of 0.414 565 Å. Discrete detectors covering an angular range from −6° to 28° 2θ are scanned over a 34° 2θ range, with data points collected every 0.001° 2θ and scan speed of 0.1° s^{-1}. All samples were prepared using the nested capillary method to avoid problem with the high absorption coefficient of PbTe. In a typical sample preparation, finely ground PbTe was coated outside a 0.80 mm Kapton capillary coated with grease. The covered hollow capillary was subsequently transferred inside a 1.50 mm Kapton capillary and held in place by adding clay on both capillary ends, before mounted on a magnetic holder base. The 11-BM instrument uses X-ray optics with two platinum-striped mirrors and a double-crystal Si(111) monochromator, where the second crystal has an adjustable sagittal bend.[71] Ion chambers monitor incident flux. A vertical Huber 480 goniometer, equipped with a Heidenhain encoder, positions an analyzer system comprised of 12 perfect Si(111) analyzers and 12 Oxford-Danfysik $LaCl_3$ scintillators, with a spacing of 2° 2θ.[72] Analyzer orientation can be adjusted individually on two axes. A three-axis translation stage holds the sample mounting and allows it to be spun at ≈5400 RPM (90 Hz). A Mitsubishi robotic arm is used to mount and dismount samples on the diffractometer.[73] The diffractometer is controlled via Experimental Physics and Industrial Control System (EPICS).[74] Data are collected, while continually scanning the diffractometer 2θ arm. A mixture of NIST standard reference materials, Si (SRM 640c) and Al_2O_3 (SRM 676) is used to calibrate the instrument, where the Si lattice constant determines the wavelength for each detector. Corrections are applied for detector sensitivity, 2θ offset, small differences in wavelength between detectors, and the source intensity, as noted by the ion chamber before merging the data into a single set of intensities evenly spaced in 2θ. Data manipulations were made using CMPR,[75] whereas full Rietveld refinements were carried out using Jana2006.[76]

Electrical Properties: The obtained SPS processed pellets were cut into bars with dimensions 12 × 3 × 3 mm^3 for simultaneous measurement of the Seebeck coefficient and electrical conductivity using an Ulvac Riko ZEM-3 instrument under a low-pressure helium atmosphere from room temperature to 900 K. The bars were spray coated with a thin layer of boron nitride to minimize outgassing except where needed for electrical contact with the thermocouples, heater, and voltage probes. The uncertainties of the Seebeck coefficient and electrical conductivity measurements are ≈5% and 10%, respectively.

Thermal Properties: Highly dense SPS processed pellets were cut and polished into a squared shape of 6 × 6 × 2 mm^3 for thermal diffusivity

measurements. The samples were spray coated with a thin layer of graphite to minimize errors from the emissivity of the material. The total thermal conductivity was calculated from $\kappa_{tot} = D \bullet C_p \bullet d$, where the thermal diffusivity coefficient (D) was measured using the laser flash diffusivity method in a Netzsch LFA457, the specific heat capacity (C_p) of $(PbTe)_{1-x}(PbS)_x$ alloy was determined by a weighted average of the temperature-dependent specific heat literature values for PbTe[77] and PbS,[78] and the density (d) was determined using the dimensions and mass of the sample. The thermal diffusivity data were analyzed using a Cowan model with pulse correction. The heat capacity and the thermal diffusion data for all samples can be found in Figures S7 and S8 (Supporting Information), respectively. The uncertainty of the thermal conductivity is estimated to be within 10%, considering all the uncertainties from D (≈5%), C_p (≈8%), and d (≈3%). The lattice thermal conductivity (κ_{lat}) is obtained by subtracting the electronic contribution (κ_{ele}) from κ_{tot} using a Wiedemann–Franz relationship $\kappa_{el} = L \bullet \sigma \bullet T$, where L is Lorenz number which can be obtained by fitting the Seebeck coefficient to the reduced chemical potential,[54] Figure S6 (Supporting Information). The combined uncertainty for all measurements involved in the calculation of ZT is around 15%. Note that error bars were not added in any figures to increase the readability of the curves. Unless otherwise noted, all the electrical and thermal properties described in this study were measured on different parts of the same pellet and perpendicular to the sintering pressure direction, although no directional anisotropy effects or composition inhomogeneity were observed in the charge transport properties.

Infrared Spectroscopy: Room temperature optical diffuse reflectance measurements were performed on finely ground powders to probe optical energy gap of the $PbTe_{1-x}S_x$. The spectra were collected in the mid-IR range (6000–400 cm^{-1}) using a Nicolet 6700 FT-IR spectrometer. The reflectance versus wavelength data generated, were used to estimate the bandgap by converting reflectance to absorption data according to Kubelka–Munk equations: $\alpha/S = (1\text{-}R)^2/(2R)$, where R is the reflectance, α and S are the absorption and scattering coefficients, respectively.

Hall Measurements: The room and high temperature Hall measurement was performed on a homemade apparatus (University of Michigan) in an argon atmosphere. The Hall resistance was monitored with a Linear Research AC Resistance Bridge (LR-700), with constant magnetic fields of ±1 T applied by using an Oxford Superconducting magnet. The effective carrier concentration (n) was estimated using the relationship $n = 1/(e \bullet R_H)$, where e is the elemental charge, and R_H is the Hall coefficient. The Hall mobility (μ_H) was calculated using the relationship $\mu_H = \sigma \bullet R_H$ with σ being the electrical conductivity obtained from ZEM-3 instrument.

Supporting Information

Supporting Information is available from the Wiley Online Library or from the author.

Acknowledgements

This work was supported by DARPA Grant HR0011-16-C-0035. Use of the Advanced Photon Source at the Argonne National Laboratory was supported by the U.S. Department of Energy, Office of Science, Office of Basic Energy Sciences, under Contract No. DE-AC02-06CH11357. The authors thank Dr. James Hodges for his valuable suggestions through the manuscript preparation.

Conflict of Interest

The authors declare no conflict of interest.

Keywords

doping, n-type PbTe, thermal conductivity, thermoelectrics

Received: January 10, 2017
Revised: March 23, 2017
Published online: May 22, 2017

[1] K. F. Hsu, S. Loo, F. Guo, W. Chen, J. S. Dyck, C. Uher, T. Hogan, E. Polychroniadis, M. G. Kanatzidis, *Science* **2004**, *303*, 818.
[2] J. R. Sootsman, D. Y. Chung, M. G. Kanatzidis, *Angew. Chem., Int. Ed.* **2009**, *48*, 8616.
[3] F. J. DiSalvo, *Science* **1999**, *285*, 703.
[4] G. Tan, L.-D. Zhao, M. G. Kanatzidis, *Chem. Rev.* **2016**, *116*, 12123.
[5] Y. Zhao, J. S. Dyck, B. M. Hernandez, C. Burda, *J. Am. Chem. Soc.* **2010**, *132*, 4982.
[6] G. Tan, S. Wang, Y. Yan, H. Li, X. Tang, *J. Alloys Compd.* **2012**, *513*, 328.
[7] R. Chasmar, R. Stratton, *Int. J. Electron.* **1959**, *7*, 52.
[8] H. Lin, G. Tan, J.-N. Shen, S. Hao, L.-M. Wu, N. Calta, C. Malliakas, S. Wang, C. Uher, C. Wolverton, M. G. Kanatzidis, *Angew. Chem., Int. Ed.* **2016**, *55*, 11431.
[9] J. P. Heremans, V. Jovovic, E. S. Toberer, A. Saramat, K. Kurosaki, A. Charoenphakdee, S. Yamanaka, G. J. Snyder, *Science* **2008**, *321*, 554.
[10] K. Biswas, J. He, Q. Zhang, G. Wang, C. Uher, V. P. Dravid, M. G. Kanatzidis, *Nat. Chem.* **2011**, *3*, 160.
[11] K. Biswas, J. He, I. D. Blum, C.-I. Wu, T. P. Hogan, D. N. Seidman, V. P. Dravid, M. G. Kanatzidis, *Nature* **2012**, *489*, 414.
[12] Y. Pei, X. Shi, A. LaLonde, H. Wang, L. Chen, G. J. Snyder, *Nature* **2011**, *473*, 66.
[13] O. Delaire, J. Ma, K. Marty, A. F. May, M. A. McGuire, M.-H. Du, D. J. Singh, A. Podlesnyak, G. Ehlers, M. Lumsden, *Nat. Mater.* **2011**, *10*, 614.
[14] S. Kastbjerg, N. Bindzus, M. Søndergaard, S. Johnsen, N. Lock, M. Christensen, M. Takata, M. A. Spackman, B. Brummerstedt Iversen, *Adv. Funct. Mater.* **2013**, *23*, 5477.
[15] S. Christensen, N. Bindzus, M. Sist, M. Takata, B. B. Iversen, *Phys. Chem. Chem. Phys.* **2016**, *18*, 15874.
[16] E. S. Božin, C. D. Malliakas, P. Souvatzis, T. Proffen, N. A. Spaldin, M. G. Kanatzidis, S. J. L. Billinge, *Science* **2010**, *330*, 1660.
[17] S. N. Girard, J. He, X. Zhou, D. Shoemaker, C. M. Jaworski, C. Uher, V. P. Dravid, J. P. Heremans, M. G. Kanatzidis, *J. Am. Chem. Soc.* **2011**, *133*, 16588.
[18] Q. Zhang, F. Cao, W. Liu, K. Lukas, B. Yu, S. Chen, C. Opeil, D. Broido, G. Chen, Z. Ren, *J. Am. Chem. Soc.* **2012**, *134*, 10031.
[19] J. Androulakis, C.-H. Lin, H.-J. Kong, C. Uher, C.-I. Wu, T. Hogan, B. A. Cook, T. Caillat, K. M. Paraskevopoulos, M. G. Kanatzidis, *J. Am. Chem. Soc.* **2007**, *129*, 9780.
[20] K. Biswas, J. He, G. Wang, S.-H. Lo, C. Uher, V. P. Dravid, M. G. Kanatzidis, *Energy Environ. Sci.* **2011**, *4*, 4675.
[21] P. Rawat, B. Paul, P. Banerji, *ACS Appl. Mater. Interfaces* **2014**, *6*, 3995.
[22] R. Allgaier, B. Houston Jr., *J. Appl. Phys.* **1966**, *37*, 302.
[23] H. Sitter, K. Lischka, H. Heinrich, *Phys. Rev. B* **1977**, *16*, 680.
[24] Y. Pei, A. D. LaLonde, N. A. Heinz, G. J. Snyder, *Adv. Energy Mater.* **2012**, *2*, 670.
[25] L. Zhao, H. Wu, S. Hao, C.-I. Wu, X. Zhou, K. Biswas, J. He, T. P. Hogan, C. Uher, C. Wolverton, *Energy Environ. Sci.* **2013**, *6*, 3346.
[26] Y. Pei, A. D. LaLonde, N. A. Heinz, X. Shi, S. Iwanaga, H. Wang, L. Chen, G. J. Snyder, *Adv. Mater.* **2011**, *23*, 5674.
[27] Y. Pei, H. Wang, Z. M. Gibbs, A. D. LaLonde, G. J. Snyder, *NPG Asia Mater.* **2012**, *4*, e28.

[28] A. Lusakowski, P. Boguslawski, T. Radzynski, *Phys. Rev. B* **2011**, *83*, 115206.
[29] Y. Takagiwa, Y. Pei, G. Pomrehn, G. Snyder, *Appl. Phys. Lett.* **2012**, *101*, 092102.
[30] L. Rogers, *Br. J. Appl. Phys.* **1967**, *18*, 1227.
[31] Y. I. Ravich, B. Efimova, V. Tamarchenko, *Phys. Status Solidi B* **1971**, *43*, 11.
[32] G. Tan, F. Shi, S. Hao, L.-D. Zhao, H. Chi, X. Zhang, C. Uher, C. Wolverton, V. P. Dravid, M. G. Kanatzidis, *Nat. Commun.* **2016**, *7*, 12167.
[33] Y. Pei, Z. M. Gibbs, A. Gloskovskii, B. Balke, W. G. Zeier, G. J. Snyder, *Adv. Energy Mater.* **2014**, *4*, 1400486.
[34] P. Jood, M. Ohta, M. Kunii, X. Hu, H. Nishiate, A. Yamamoto, M. G. Kanatzidis, *J. Mater. Chem. C* **2015**, *3*, 10401.
[35] Q. Zhang, E. K. Chere, Y. Wang, H. S. Kim, R. He, F. Cao, K. Dahal, D. Broido, G. Chen, Z. Ren, *Nano Energy* **2016**, *22*, 572.
[36] S. N. Girard, T. C. Chasapis, J. He, X. Zhou, E. Hatzikraniotis, C. Uher, K. M. Paraskevopoulos, V. P. Dravid, M. G. Kanatzidis, *Energy Environ. Sci.* **2012**, *5*, 8716.
[37] Y. Gelbstein, Z. Dashevsky, M. Dariel, *Phys. B* **2005**, *363*, 196.
[38] X. Xuan, *Semicond. Sci. Technol.* **2002**, *17*, 114.
[39] T. Tavrina, E. Rogacheva, V. Pinegin, *Mold. J. Phys. Sci* **2005**, *4*, 430.
[40] C. M. Jaworski, J. Tobola, E. Levin, K. Schmidt-Rohr, J. P. Heremans, *Phys. Rev. B* **2009**, *80*, 125208.
[41] A. Strauss, *J. Electron. Mater.* **1973**, *2*, 553.
[42] R. D. Shannon, *Acta Crystallogr., Sect. A: Found. Adv.* **1976**, *32*, 751.
[43] O. Madelung, in *Semiconductors: Data Handbook*, Springer, Berlin, Heidelberg, **2004**, p. 173.
[44] D. Zayachuk, *Semiconductors* **1997**, *31*, 173.
[45] D. Freik, S. Mudryi, I. Gorichok, R. Dzumedzey, O. Krynytskyi, T. Lyuba, O. S. Krynytskyi, T. S. Lyuba, *Ukr. J. Phys.* **2014**, *59*, 706.
[46] Y. Lee, S.-H. Lo, C. Chen, H. Sun, D.-Y. Chung, T. C. Chasapis, C. Uher, V. P. Dravid, M. G. Kanatzidis, *Nat. Commun.* **2014**, *5*, 3640.
[47] S. Aminorroaya Yamini, H. Wang, D. Ginting, D. R. G. Mitchell, S. X. Dou, G. J. Snyder, *ACS Appl. Mat. Interfaces* **2014**, *6*, 11476.
[48] G. Meisner, D. Morelli, S. Hu, J. Yang, C. Uher, *Phys. Rev. Lett.* **1998**, *80*, 3551.
[49] G. Tan, W. G. Zeier, F. Shi, P. Wang, G. J. Snyder, V. P. Dravid, M. G. Kanatzidis, *Chem. Mater.* **2015**, *27*, 7801.
[50] G. Tan, S. Wang, X. Tang, *J. Electron. Mater.* **2014**, *43*, 1712.
[51] Y. Pei, J. Lensch-Falk, E. S. Toberer, D. L. Medlin, G. J. Snyder, *Adv. Funct. Mater.* **2011**, *21*, 241.
[52] G. Tan, L.-D. Zhao, F. Shi, J. W. Doak, S.-H. Lo, H. Sun, C. Wolverton, V. P. Dravid, C. Uher, M. G. Kanatzidis, *J. Am. Chem. Soc.* **2014**, *136*, 7006.
[53] G. Tan, F. Shi, H. Sun, L.-D. Zhao, C. Uher, V. P. Dravid, M. G. Kanatzidis, *J. Mater. Chem. A* **2014**, *2*, 20849.
[54] G. Tan, W. Liu, H. Chi, X. Su, S. Wang, Y. Yan, X. Tang, W. Wong-Ng, C. Uher, *Acta Mater.* **2013**, *61*, 7693.
[55] G. Tan, W. Liu, S. Wang, Y. Yan, H. Li, X. Tang, C. Uher, *J. Mater. Chem. A* **2013**, *1*, 12657.
[56] G. Tan, H. Chi, W. Liu, Y. Zheng, X. Tang, J. He, C. Uher, *J. Mater. Chem. C* **2015**, *3*, 8372.
[57] Y.-L. Pei, Y. Liu, *J. Alloys Compd.* **2012**, *514*, 40.
[58] S. N. Girard, K. Schmidt-Rohr, T. C. Chasapis, E. Hatzikraniotis, B. Njegic, E. M. Levin, A. Rawal, K. M. Paraskevopoulos, M. G. Kanatzidis, *Adv. Funct. Mater.* **2013**, *23*, 747.
[59] J. He, I. D. Blum, H.-Q. Wang, S. N. Girard, J. Doak, L.-D. Zhao, J.-C. Zheng, G. Casillas, C. Wolverton, M. Jose-Yacaman, D. N. Seidman, M. G. Kanatzidis, V. P. Dravid, *Nano Lett.* **2012**, *12*, 5979.
[60] P. Klemens, *Phys. Rev.* **1960**, *119*, 507.
[61] J. Androulakis, I. Todorov, J. He, D.-Y. Chung, V. Dravid, M. Kanatzidis, *J. Am. Chem. Soc.* **2011**, *133*, 10920.
[62] G. Alekseeva, B. Efimova, L. Ostrovskaya, O. Serebryannikova, M. Tsypin, *Sov. Phys.: Semicond.* **1971**, *4*, 1122.
[63] G. Tan, F. Shi, S. Hao, H. Chi, T. P. Bailey, L.-D. Zhao, C. Uher, C. Wolverton, V. P. Dravid, M. G. Kanatzidis, *J. Am. Chem. Soc.* **2015**, *137*, 11507.
[64] G. Tan, F. Shi, J. W. Doak, H. Sun, L.-D. Zhao, P. Wang, C. Uher, C. Wolverton, V. P. Dravid, M. G. Kanatzidis, *Energy Environ. Sci.* **2015**, *8*, 267.
[65] S. Johnsen, J. He, J. Androulakis, V. P. Dravid, I. Todorov, D. Y. Chung, M. G. Kanatzidis, *J. Am. Chem. Soc.* **2011**, *133*, 3460.
[66] H. Wang, E. Schechtel, Y. Pei, G. J. Snyder, *Adv. Energy Mater.* **2013**, *3*, 488.
[67] I. I. Ravich, *Semiconducting Lead Chalcogenides*, Vol. *5*, Springer Science & Business Media, New York, **2013**.
[68] X. Shi, J. Yang, J. R. Salvador, M. Chi, J. Y. Cho, H. Wang, S. Bai, J. Yang, W. Zhang, L. Chen, *J. Am. Chem. Soc.* **2011**, *133*, 7837.
[69] W. Liu, X. Tan, K. Yin, H. Liu, X. Tang, J. Shi, Q. Zhang, C. Uher, *Phys. Rev. Lett.* **2012**, *108*, 166601.
[70] V. Leute, N. Volkmer, *Z. Phys. Chem.* **1985**, *144*, 145.
[71] J. Wang, B. H. Toby, P. L. Lee, L. Ribaud, S. Antao, C. Kurtz, M. Ramanathan, R. B. Von Dreele, M. A. Beno, *Rev. Sci. Instrum.* **2008**, *79*, 085105.
[72] P. L. Lee, D. Shu, M. Ramanathan, C. Preissner, J. Wang, M. A. Beno, R. B. Von Dreele, L. Ribaud, C. Kurtz, S. M. Antao, X. Jiao, B. H. Toby, *J. Synchrotron Radiat.* **2008**, *15*, 427.
[73] C. Preissner, D. Shu, B. H. Toby, P. Lee, J. Wang, D. Kline, K. Goetze, *Nucl. Instrum. Methods Phys. Res., Sect. A* **2009**, *42*, 990.
[74] L. R. Dalesio, J. O. Hill, M. Kraimer, S. Lewis, D. Murray, S. Hunt, W. Watson, M. Clausen, J. Dalesio, *Nucl. Instrum. Methods Phys. Res., Sect. A* **1994**, *352*, 179.
[75] B. Toby, *J. Appl. Crystallogr.* **2005**, *38*, 1040.
[76] V. Petříček, M. Dušek, L. Palatinus, *Z. Kristallogr. - Cryst. Mater.* **2014**, *229*, 345.
[77] A. Pashinkin, M. Mikhailova, A. Malkova, V. Fedorov, *Inorg. Mater.* **2009**, *45*, 1226.
[78] R. Blachnik, R. Igel, Z. Naturforsch, *B: Anorg. Chem., Org. Chem.* **1974**, *29*, 625.

